SIMULI: REAL-TIME LIDAR AND CAMERA SIMULATION WITH UNSCENTED TRANSFORMS

Anonymous authors
Paper under double-blind review

ABSTRACT

Rigorous testing of autonomous robots, such as self-driving vehicles, is essential to ensure their safety in real-world deployments. This requires building high-fidelity simulators to test scenarios beyond those that can be safely or exhaustively collected in the real-world. Existing neural rendering methods based on NeRF and 3DGS hold promise but suffer from low rendering speeds or can only render pinhole camera models, hindering their suitability to applications that commonly require high-distortion lenses and LiDAR data. Multi-sensor simulation poses additional challenges as existing methods handle cross-sensor inconsistencies by favoring the quality of one modality at the expense of others. To overcome these limitations, we propose SimULi, the first method capable of rendering arbitrary camera models and LiDAR data in real-time. Our method extends 3DGUT, which natively supports complex camera models, with LiDAR support, via an automated tiling strategy for arbitrary spinning LiDAR models and ray-based culling. To address cross-sensor inconsistencies, we design a factorized 3D Gaussian representation and anchoring strategy that reduces mean camera and depth error by up to 40% compared to existing methods. SimULi renders 10-20× faster than ray tracing approaches and 1.5-14× faster than prior rasterization-based work (and handles a wider range of camera models). When evaluated on two widely benchmarked autonomous driving datasets, SimULi matches or exceeds the fidelity of existing state-of-the-art methods across numerous camera and LiDAR metrics.

Figure 1: **SimULi.** We design a factorized 3D Gaussian representation that encodes camera and LiDAR information into separate sets of 3D Gaussians joined via nearest-neighbor anchoring loss (**left**). To efficiently render LiDAR scans (**middle**), we extend 3DGUT (Wu et al., 2025b) with an automated tiling strategy and ray-based culling. When compared to existing methods, we render 1.5-20× faster and match or exceed LiDAR and camera quality (**right**) across a wide range of metrics.

1 INTRODUCTION

With the rise of end-to-end policy models, accurate sensor simulation has become a critical component in the development and evaluation of autonomous vehicle (AV) systems. Data-driven meth-

ods based on Neural Radiance Fields (NeRFs) (Mildenhall et al., 2020) offer a scalable solution for reconstructing high-quality, diverse simulation environments directly from real-world sensor data (Turki et al., 2023; Yang et al., 2023b). As they are optimized to match real-world observations, they also exhibit a smaller domain gap compared to traditional artist-generated simulators.

Multi-Sensor Simulation. In addition to cameras, most AVs are equipped with active sensors such as LiDAR to obtain 3D measurements of their surroundings. Early approaches focus on camera simulation (Rematas et al., 2022), using other sensors to constrain geometry for improved novel view synthesis, or solely on LiDAR (Tao et al., 2023; Huang et al., 2023). Recent efforts (Yang et al., 2023b; Tonderski et al., 2024; Hess et al., 2025) jointly model both sensors, a challenging task as cross-sensor calibration inconsistencies due are impossible to eliminate in the real world. In practice, they are forced to prioritize camera quality at the cost of LiDAR accuracy (or vice-versa).

Sensor Rendering. NeRF-based methods (Yang et al., 2023b; Tonderski et al., 2024) suffer from low rendering speeds, limiting their practicality for large-scale use. Replacing NeRFs with a 3D Gaussian Splatting (3DGS) formulation (Kerbl et al., 2023) mitigates these challenges by enabling real-time rendering through a rasterization-based pipeline, while maintaining, or even improving, visual fidelity, especially for larger scenes (Chen et al., 2025; Yan et al., 2024; Zhou et al., 2024).

However, this comes at the cost of limitations inherent to the rasterization paradigm. In particular, rasterization is constrained to idealized pinhole camera models and does not naturally support non-linear projection functions (e.g., fisheye lenses) or time-dependent effects such as rolling shutter, both of which are common in data captured by AV sensor suites (Xiao et al., 2021; Sun et al., 2020; Caesar et al., 2020; Wilson et al., 2021; Liao et al., 2021). Rectifying training images and ignoring rolling shutter effects degrades reconstruction quality, while the inability to render non-pinhole camera views introduces a significant domain gap for downstream models, which are typically trained on raw sensor data. LiDAR sensors are often neglected, as their sparse, irregular sampling pattern and strong time-dependent effects make them difficult to model within the 3DGS framework.

SimULi. In this work, we propose a high-fidelity and efficient reconstruction pipeline that enables joint camera and LiDAR simulation for AV scenarios. Importantly we aim to: **(i)** natively support arbitrary camera and LiDAR models, including their time-dependent effects; **(ii)** accurately model sensor characteristics (such as color, LiDAR intensity, and ray drop effects), without prioritizing the accuracy of one sensor at the expense of others as in existing work; and **(iii)** achieve real-time inference while maintaining high visual fidelity.

We build upon the 3D Gaussian Unscented Transform (3DGUT) (Wu et al., 2025b), which inherently supports non-linear camera models and time-dependent effects such as rolling shutter. In this work, we extend it further to support rotating LiDAR sensors with irregular sampling patterns. Specifically, we **(i)** derive a LiDAR measurement model that accounts for its time-dependent behavior, **(ii)** introduce a histogram-equalization-based algorithm to compute an optimal tiling scheme for handling the highly irregular structure of LiDAR measurements, and **(iii)** take advantage of the relative sparsity of LiDAR rays via a culling strategy that further accelerates rendering.

To accurately model multi-sensor data, we encode the information relevant to each modality into distinct sets of 3D Gaussians coupled via an efficient nearest-neighbor anchoring method. We derive several benefits. First, we find that this handles cross-sensor inconsistencies far more robustly than prior methods that encode all sensor data into a single NeRF (Yang et al., 2023b; Tonderski et al., 2024) or set of Gaussian particles (Hess et al., 2025), allowing us to match or exceed the accuracy of camera-only or LiDAR-only simulation. Second, this improves rendering efficiency, as the information needed to render each sensor is contained within a subset of Gaussians (accelerating LiDAR rendering by 2-3$\times$). Third, by specializing the characteristics of each Gaussian set, we benefit from inductive biases inherent to each sensor. Since LiDAR returns typically intersect surfaces, we encourage sparsity and binary opacity in LiDAR Gaussians, further improving rendering speed. Camera Gaussians remain unconstrained and benefit from the smooth optimization properties and high rendering quality of volumetric approaches (Wang et al., 2023; Turki et al., 2024).

Contributions. We make the following contributions: (1) we extend 3DGUT with LiDAR support and introduce an automated tiling scheme from which we derive optimal tiling parameters for any spinning LiDAR model without relying on handcrafted heuristics (Hess et al., 2025), (2) we design

a factorized 3D Gaussian representation and anchoring strategy that mitigates the camera vs LiDAR accuracy tradeoff needed in prior methods, (3) we present results that surpass existing LiDAR and camera-based SOTA, without relying on neural networks for refinement as in prior NeRF (Tonderski et al., 2024; Yang et al., 2023b; Zheng et al., 2024) and 3DGS-based work (Zhou et al., 2025; Hess et al., 2025). Our simplified approach renders 1.5-14$\times$ faster than recent rasterization-based methods (Hess et al., 2025), 10-20$\times$ faster than ray tracing approaches (Zhou et al., 2025), and is, to our knowledge, the first to render in real-time and support arbitrary camera and LiDAR models.

2 Related Work

Recent neural reconstruction methods (Mildenhall et al., 2020; Kerbl et al., 2023) have greatly influenced AV simulation by enabling the reconstruction of large, high-fidelity environments from raw sensor data. We list a non-exhaustive selection of these methods along axes most relevant to ours.

Simulating Camera Observations. Early neural reconstruction methods in the AV domain focused on modeling camera observations (Ost et al., 2021; Xie et al., 2023; Guo et al., 2023; Yang et al., 2023a), often leveraging LiDAR data to constrain geometry and enhance novel view synthesis. To adapt static NeRF representations to the AV setting, these approaches introduced domain-specific extensions such as dynamic scene graph parameterizations (Ost et al., 2021) and specialized sky representations (Guo et al., 2023; Yang et al., 2023a). With the advent of 3DGS (Kerbl et al., 2023), which enables faster rendering and better scalability, several of these ideas have been reimplemented within particle-based representations (Chen et al., 2025; Yan et al., 2024; Chen et al., 2023). While 3DGS-based methods yield faster frame rates, they also inherit all the limitations of rasterization.

Simulating LiDAR Observations. In parallel to camera-focused approaches, several works have adapted neural reconstruction methods for LiDAR novel view synthesis (Huang et al., 2023; Tao et al., 2023; Zhang et al., 2024). NFL (Huang et al., 2023) introduced a physically grounded way of modeling LiDAR characteristics within NeRFs. DyNFL (Wu et al., 2024) and LiDAR4D (Zheng et al., 2024) extended NFL to dynamic scenes using the same scene graph parameterization as camera methods and improve rendering speed via acceleration structures (Müller et al., 2022).

Adapting 3DGS for LiDAR rendering is more challenging, as its rasterization assumes ideal pinhole camera models and its tiling strategy does not naturally accommodate the non-uniform sampling patterns of LiDAR sensors. Recently, 3DGRT (Moenne-Loccoz et al., 2024) replaced rasterization with a ray tracing formulation, enabling support for more complex sensor models. LiDAR-RT (Zhou et al., 2025) applies this framework specifically to LiDAR simulation, while GS-LiDAR (Jiang et al., 2025) combines a similar method with tile-based panoramic rendering. Both approaches render faster than NeRF-based approaches but remain several times slower than rasterization methods.

Joint LiDAR-Camera Simulation. Recent works jointly model LiDAR and camera novel view synthesis via a unified neural representation. UniSim (Yang et al., 2023b) and NeuRAD (Tonderski et al., 2024) build upon NeRF and adapt the rendering formulation for different sensors using the same underlying model. AlignMiF (Tang et al., 2024) encodes sensors into separate feature grids aligned via shared initialization and feature fusion. They remain impractical due to the slow rendering speed of NeRF and (other than AlignMiF) perform worse than camera-only or LiDAR reconstruction due to cross-sensor inconsistencies.

Closest to our work, SplatAD (Hess et al., 2025) extends 3DGS with a LiDAR rendering formulation that supports non-uniform sampling patterns (as does ours) and support for rolling shutter effects. While it addresses several important challenges, it differs from our method in three key aspects. First, as a 3DGS-based method, it remains limited to perfect pinhole camera models, whereas SimULi builds upon 3DGUT (Wu et al., 2025b), which enables native support for high-distortion camera models, such as fisheye lenses. Second, it relies on manual heuristics to determine the tiling strategy for each LiDAR sensor. In contrast, we demonstrate how an automated strategy can adaptively compute optimal tiling patterns across a wide range of non-uniform LiDAR sensors. Third, it encodes all sensor information into the same Gaussian set, and suffers from cross-sensor inconsistencies as prior NeRF-based works (Tonderski et al., 2024; Yang et al., 2023b), which we mitigate by encoding each sensor into its own particle set and using an anchoring loss. We illustrate the difference in approaches via extensive benchmarking in Sec. 4.

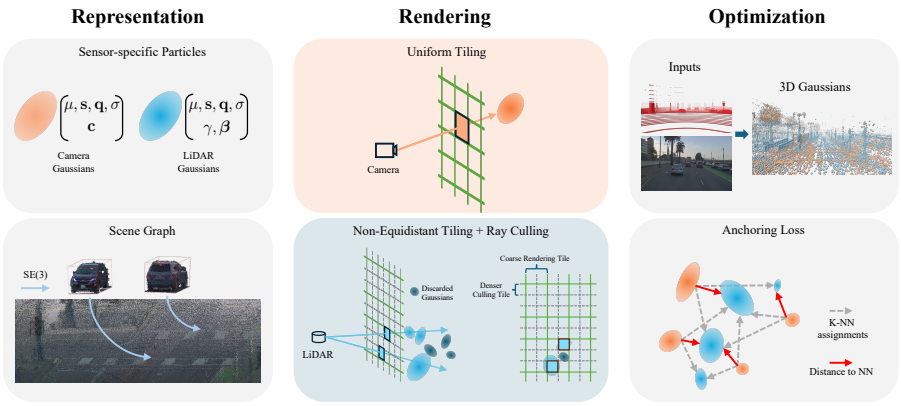

Figure 2: **Method Overview.** We model the scene as a dynamic graph (Ost et al., 2021) and parameterize the background and each actor with camera and LiDAR 3D Gaussians (**left**). We render camera views similar to 3DGUT (Wu et al., 2025b) and derive an automated tiling strategy and ray-based culling to efficiently render LiDAR (**middle**). We sample an image and LiDAR scan at each training step to optimize our representation (**right**). To improve camera novel view synthesis with LiDAR-supervised geometry, we anchor camera Gaussians near surfaces via nearest-neighbor loss.

3 METHOD

Our goal is to learn a controllable scene representation that simulates camera and LiDAR renderings from novel viewpoints in real-time (Fig. 2). We describe our representation in Sec. 3.1, our general rendering approach in Sec. 3.2, LiDAR specifically in Sec. 3.3, and optimization in Sec. 3.4.

3.1 REPRESENTATION

Particle Representation. We encode camera and LiDAR attributes into separate unordered sets G_c and G_l of semi-transparent 3D Gaussian particles (Kerbl et al., 2023). Particles in both sets are parameterized by their 3D position $\boldsymbol{\mu}_i \in \mathbb{R}^3$, opacity coefficient $\sigma \in \mathbb{R}$, and covariance matrix $\boldsymbol{\Sigma}_i \in \mathbb{R}^{3\times3}$. $\boldsymbol{\Sigma}_i$ is decomposed into a rotation matrix $\mathbf{R} \in \mathrm{SO}(3)$ and a scaling matrix $\mathbf{S} \in \mathbb{R}^{3\times3}$, such that $\boldsymbol{\Sigma} = \mathbf{RSS}^T\mathbf{R}^T$, to ensure that it remains positive semi-definite. We associate 3^{rd}-order spherical harmonics coefficients $\mathbf{SH^c} \in \mathbb{R}^{48}$ to camera Gaussians to encode view-dependent color, and $\mathbf{SH^l} \in \mathbb{R}^{48}$ to LiDAR Gaussians for view-dependent intensity and ray drop information.

Scene Representation. We adopt a graph decomposition similar to prior work (Ost et al., 2021) to enable controllability in dynamic scenes. We assign each particle in G_c and G_l to a dynamic object or the static background. Each object is associated with a 3D bounding box and a sequence of $\mathrm{SE}(3)$ poses adjusted with learnable offsets. The means and covariances of the Gaussians assigned to objects are expressed in the objects' local coordinate system. At render time, they are transformed to world coordinates by applying the $\mathrm{SE}(3)$ transformation corresponding to the timestamp t.

3.2 RENDERING

We build our differentiable renderer upon 3DGUT (Wu et al., 2025b), as it supports complex cameras and time-dependent effects that are common in autonomous driving data.

Volume Rendering. Given a camera ray $\mathbf{r}(\tau) = \mathbf{o} + \tau\mathbf{d}$ with origin $\mathbf{o} \in \mathbb{R}^3$ and direction $\mathbf{d} \in \mathbb{R}^3$, we volumetrically render a foreground color $\mathbf{c_f} \in \mathbb{R}^3$ and opacity $\omega \in \mathbb{R}$ via numerical integration over the interacting Gaussian particles in G_c:

$$\mathbf{c_f}(\mathbf{o},\mathbf{d}) = \sum_{i\in G_c} \mathbf{SH}_i^{\mathbf{c}}(\mathbf{d})\alpha_i T_i, \quad \omega(\mathbf{o},\mathbf{d}) = \sum_{i\in G_c} \alpha_i T_i, \quad \alpha_i = \sigma_i \rho_i(\mathbf{o}+\tau\mathbf{d}), \quad T_i = \prod_{j=1}^{i-1} 1-\alpha_j, \tag{1}$$

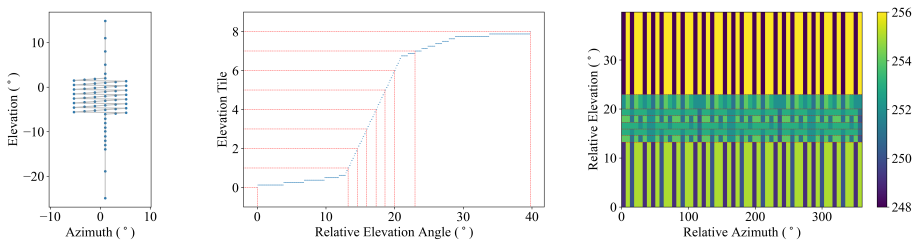

(a) Beam pattern (b) Elevation angle to tile map (c) Beam count per tile

Figure 3: **LiDAR Tiling.** As the measurement pattern of commonly used LiDAR sensors (Xiao et al., 2021) is irregular (**left**), rendering with equally spaced tiles is highly inefficient. We compute the normalized CDF of elevation angles using a predefined histogram bin count and set elevation tiling boundaries at angles where the CDF values cross integer boundaries (**middle**). We then compute an azimuth tile count such that the beam count per tile differs at most by 8 samples (**right**).

where ρ_i is the particle response described in the next paragraph. We alpha-composite the foreground color $\mathbf{c_f}$ with a background color $\mathbf{c_b}$ obtained from a learned texture environment map (Chen et al., 2023; 2025). We obtain the final color prediction $\mathbf{c}$ via an affine transformation from a learned bilateral grid $\mathcal{A}$ (Wang et al., 2024) that handles lighting variations across frames and cameras:

$$\mathbf{c}(\mathbf{o},\mathbf{d}) = \mathcal{A}(\omega(\mathbf{o},\mathbf{d})\mathbf{c_f}(\mathbf{o},\mathbf{d}) + (1-\omega(\mathbf{o},\mathbf{d}))\mathbf{c_b}(\mathbf{d})) \tag{2}$$

We similarly render LiDAR features $\zeta \in \mathbb{R}^3$ from particles in G_l as $\zeta(\mathbf{o},\mathbf{d}) = \sum_{i\in G_l} \mathbf{SH}_i^1(\mathbf{d})\alpha_i T_i$. We decode beam intensity $\gamma \in \mathbb{R}$ from the first channel of ζ and derive a ray drop probability $\beta \in \mathbb{R}$ by applying the softmax function on the remaining two channels ($\beta_{\text{hit}}, \beta_{\text{drop}}$) of ζ (Zhou et al., 2025).

Particle Contributions and Response. As in 3DGUT (Wu et al., 2025b), we determine which particles contribute to each ray by approximating each Gaussian via the Unscented Transform (UT). We project 7 sigma points per Gaussian to estimate a 2D conic $\mathbf{\Sigma}'$ before applying tiling and culling as in 3DGS (Kerbl et al., 2023). As sigma points are independently projected, we trivially handle time-dependent effects such as rolling-shutter by incorporating camera motion into the projection function (Fig. 10). We measure the particle response function of each Gaussian in 3D via the distance $\tau_{max} := \text{argmax}_\tau \rho_i(\mathbf{o}+\tau\mathbf{d})$ that maximizes its response ρ along the ray $\mathbf{r}(\tau)$ (Moenne-Loccoz et al., 2024).

3.3 LiDAR Rendering

Projection. For a given LiDAR Gaussian in G_l, we project each of its 7 sigma points onto a 2D azimuth/elevation grid. We convert the 3D Euclidean coordinates of each sigma point from the world frame to the sensor frame and derive the corresponding spherical coordinates:

$$\phi = \arctan2(y,x),\ \ \omega = \arcsin(z/r),\ \ r = \sqrt{x^2+y^2+z^2} \tag{3}$$

where ϕ denotes the azimuth, ω the elevation and r the range. We derive a 2D conic from the projected coordinates to use for tiling and culling, and handle time-dependent effects (such as the LiDAR-equivalent of rolling shutter) in the same manner as with camera rendering.

Tiling. Effectively distributing work across tiles is crucial to achieving high rendering speeds. However, unlike cameras, the resolution of LiDAR measurements is irregular and differs greatly across dimensions (Fig. 3a). Although azimuths cover the full $360°$ radius, the elevation angle is usually much smaller (around $20°$). Using equally sized tiles as with cameras is thus highly inefficient. We derive an automated strategy that takes elevation angles as input and computes an equalized elevation tiling and azimuth tile count such that each elevation tile contains roughly the same number of measurements and that the count per tile is under a user-defined constraint M.

We compute the normalized cumulative distribution function $\boldsymbol{C}$ using a pre-defined histogram bin count $r = 400$ (Fig. 3b). We then set elevation tiling boundaries at elevation angles where the corresponding cumulative distribution function values cross integer boundaries. We finally compute the

Figure 4: **Depth Supervision.** Prior work encodes camera and LiDAR into the same representation constrained with a LiDAR-supervised depth loss. As cross-sensor data is not fully consistent, this forces the representation to prioritize camera instead of LiDAR quality (**left**) or the inverse (**middle**), as shown by PSNR and chamfer distance. We factorize each modality into its own particle set joined via nearest-neighbor anchoring loss, improving the quality of each (**right**).

azimuth tile count and the maximum point count per tile constraint M. We use the azimuth tile count to uniformly tile points along the azimuth axis. This procedure happens once per sensor definition and we reuse the same tiling across rasterization calls. We provide pseudo-code in Procedure 1.

Ray-based Culling. Compared to cameras, LiDAR scans consist of fewer rays that cover a wider field of view. This results in a sparser pattern where naive tile-based rendering suffers from evaluating numerous Gaussians that that do not contribute to any rays. To address this, we use two separate tile resolutions for rendering and culling T_r and T_c, adopting a denser resolution for the latter to cull as many particles as possible ($r^d_\phi = 1600$, $r^d_\omega = 8$). After projecting a particle to the LiDAR angle space, we compute its extent in T_c, check if it is intersected by any rays, and only include the particle for rendering (using its coarse extent in T_r) if so. We filter in constant time (4 memory reads + 3 arithmetic operations) via a 2D range query where we first construct a 2D ray mask indicating whether rays intersect each culling tile and then build a summed-area table using 2D prefix sum. We provide details in Sec. C of the appendix.

Beam Divergence. LiDAR beams have a larger footprint than that of camera rays and diverge significantly as they travel away from the sensor. This causes "bloating" artifacts that are noticeable around reflective surfaces such as traffic signs where only a small portion of the beam hitting the surface is sufficient to obtain a return. These spurious returns (that a true zero-thickness ray would "miss") negatively impact the learned scene geometry when unaccounted for. To address this, we use a 3D smoothing filter similar to AAA-Gaussians (Steiner et al., 2025) but with an important modification to avoid degrading depth. We provide details in Sec. D of the appendix.

3.4 Optimization

We jointly optimize the camera particles G_c, LiDAR particles G_l, bilateral grids $\mathcal{A}$, and the environment map by sampling a random input image and LiDAR scan at each training step. We minimize a reconstruction loss, an anchoring loss that encourages camera Gaussians in G_c to lie near the LiDAR-supervised scene geometry distilled into G_l, and lower-level regularization terms such that the final loss is $\mathcal{L} \coloneqq \mathcal{L}_{recon} + \lambda_{anchor}\mathcal{L}_{anchor} + \mathcal{L}_{reg}$, with $\lambda_{anchor} = 0.01$.

Reconstruction Losses. We minimize $\mathcal{L}_{recon}$ via L1 photometric loss $\mathcal{L}_{\text{photo}}$, SSIM loss $\mathcal{L}_{\text{SSIM}}$, L1 distance loss $\mathcal{L}_{\text{dist}}$, L1 intensity loss $\mathcal{L}_{\text{int}}$, and binary cross-entropy ray drop loss $\mathcal{L}_{\text{rd}}$:

$$\mathcal{L}_{recon} = \underbrace{\left(\lambda_{photo}\mathcal{L}_{photo} + \lambda_{SSIM}\mathcal{L}_{SSIM}\right)}_{\text{camera losses}} + \underbrace{\left(\lambda_{dist}\mathcal{L}_{dist} + \lambda_{int}\mathcal{L}_{int} + \lambda_{rd}\mathcal{L}_{rd}\right)}_{\text{LiDAR losses}}, \tag{4}$$

with $\lambda_{photo} = 0.8$, $\lambda_{SSIM} = 0.2$, $\lambda_{dist} = 0.01$, $\lambda_{int} = 0.1$, and $\lambda_{rd} = 0.05$. Camera losses only require rendering and backpropagating through particles in G_c (and LiDAR losses through G_l).

Anchoring Loss. Existing methods encode camera and LiDAR data into a single NeRF (Yang et al., 2023b; Tonderski et al., 2024) or set of 3D Gaussian particles (Hess et al., 2025). As cross-sensor data contains inconsistencies that are impossible to eliminate, this forces the representation to prioritize the reconstruction quality of one modality over the other based on loss weights (Fig. 4).

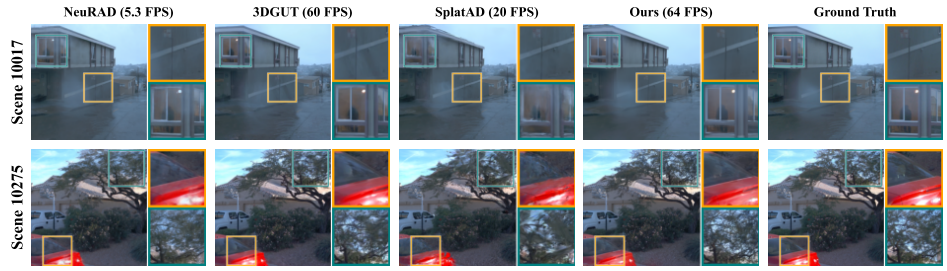

Figure 5: **Static NVS.** Our bilateral grids prevent floaters such as those 3DGUT spawns near the traffic sign (**above**), allowing us to render slightly faster. SplatAD's CNN does not properly recover the silhouette behind the window (**above**) or rear car seat (**below**), while our simpler pipeline does.

Table 1: **Waymo Interp.** SimULi renders the fastest, outperforms all baselines by >2dB PSNR, and gives better depth reconstruction than LiDAR-only LiDAR-RT (Zhou et al., 2025).

Method	PSNR↑	SSIM↑	LPIPS↓	MedL2. ↓	MeanRelL2↓	Int. RMSE↓	RayDrop↑	CD ↓	MP/s↑	MR/s↑
Nerfacto (Tancik et al., 2023)	21.79	0.516	0.734	0.164	0.035	—	—	0.523	0.77	0.80
3DGRT (Moenne-Loccoz et al., 2024)	27.49	0.860	0.264	0.008	0.009	—	—	0.196	3.23	1.39
3DGUT (Wu et al., 2025b)	27.20	0.858	0.271	24.5	0.464	—	—	5.070	148.4	—
OmniRe (Chen et al., 2025)	26.68	0.833	0.256	0.173	0.167	—	—	0.560	24.15	—
StreetGS Yan et al. (2024)	26.59	0.832	0.256	0.145	0.180	—	—	0.566	24.85	—
PVG Chen et al. (2023)	27.19	0.838	0.303	11.97	2.148	—	—	3.766	6.65	—
DeformableGS Yang et al. (2024)	27.95	0.856	0.235	0.090	0.169	—	—	0.523	5.27	—
LiDAR-RT (Zhou et al., 2025)	—	—	—	0.005	0.016	0.065	**0.962**	0.169	—	1.39
UniSim (Yang et al., 2023b)	23.17	0.756	0.369	0.056	0.041	0.077	0.823	0.456	8.32	0.98
AlignMiF (Tang et al., 2024)	24.22	0.777	0.488	0.005	0.036	0.064	0.904	0.148	0.20	0.20
NeuRAD (Tonderski et al., 2024)	27.49	0.810	**0.227**	0.005	0.049	**0.061**	0.907	0.165	13.21	1.62
SplatAD (Hess et al., 2025)	27.82	0.839	0.246	0.008	0.013	**0.061**	0.916	0.175	49.98	2.40
SimULi	**30.15**	**0.881**	0.241	**0.003**	**0.007**	0.064	0.944	**0.136**	**156.90**	**11.33**

By encoding each sensor into its own particle set against which we apply separate reconstruction losses, avoiding this tradeoff is trivial. We still wish to improve camera novel view synthesis via LiDAR-constrained geometry, and thus minimize the distance of camera Gaussians from the predicted surfaces distilled into G_l. We define a nearest-neighbor anchoring loss on Gaussian means:

$$\mathcal{L}_{anchor} = \frac{1}{n}\sum_{i \in G_c}^{n} \|\boldsymbol{\mu}_i - NN(\boldsymbol{\mu}_i, G_l)\|_2, \quad NN(\boldsymbol{\mu}, G) = argmin_{\boldsymbol{\mu}' \in G}\|\boldsymbol{\mu} - \boldsymbol{\mu}'\|_2 \tag{5}$$

Since running full nearest-neighbors on all Gaussians in G_c and G_l is computationally expensive, we assign each Gaussian in G_c to its $K = 50$ nearest neighbors in G_l. We minimize the K-distance loss at each training iteration, and update the camera-to-LiDAR assignments every 1000 iterations. Compared to the direct LiDAR-supervised depth loss used in prior work, this strategy allows the model a greater degree of freedom in addressing cross-sensor inconsistencies while still improving camera rendering via LiDAR-constrained scene geometry. We ablate its effectiveness in Sec. 4.3.

Regularization. As LiDAR is typically reflected by surfaces, we apply an entropy loss to G_l that encourages binary opacity and sparsification. To generate plausible renderings at novel timestamps, we enforce smoothness across our affine color transformations $\mathcal{A}$ and background, and regularize Gaussian scale and opacity as in MCMC (Kheradmand et al., 2024). We provide details in Sec. E.

4 Experiments

We validate the effectiveness of our method on two commonly used AV datasets across camera-only, LiDAR-only, and joint camera-LiDAR baselines. To measure against the widest possible set of baselines , we first measure novel view synthesis on static scenes used to evaluate prior work (Huang et al., 2023) (Sec. 4.1). As dynamic simulation is our main focus, we evaluate both reconstruction and novel view synthesis in Sec. 4.2. We validate the efficacy of our components in Sec. 4.3.

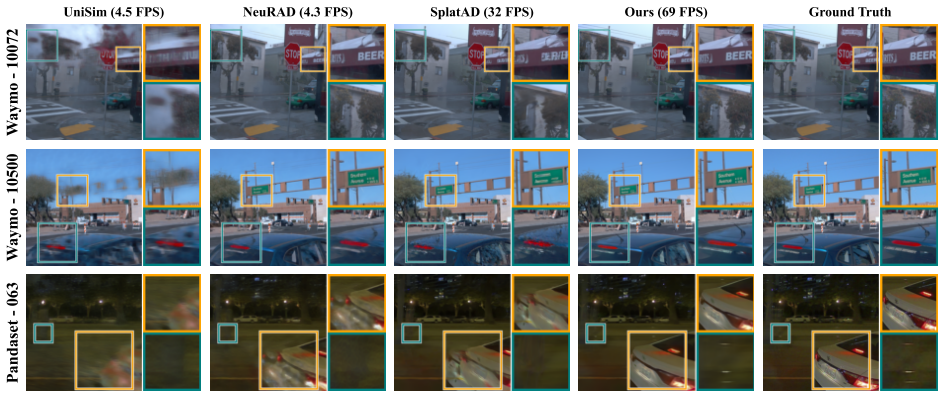

Figure 6: **Dynamic Scenes.** Methods that use CNNs for upsampling (Yang et al., 2023b; Tonderski et al., 2024) or view dependence (Hess et al., 2025) struggle with blurriness and incorrect lettering (**top rows**). Our rolling shutter strategy handles rapid movement that SplatAD's does not (**below**).

Table 2: **Waymo Dynamic.** As with static reconstruction (Table 1), we render the fastest and report best or next-best results across every camera and LiDAR metric.

Method	PSNR↑	SSIM↑	LPIPS↓	MedL2. ↓	MeanRelL2↓	Int. RMSE↓	RayDropAcc↑	CD ↓	MP/s↑	MR/s↑
OmniRe (Chen et al., 2025)	29.45	0.897	0.162	1.188	1.013	—	—	0.986	44.56	—
StreetGS Yan et al. (2024)	29.60	0.898	0.161	1.280	0.739	—	—	1.361	52.34	—
PVG Chen et al. (2023)	28.83	0.884	0.220	4.53	3.543	—	—	3.061	15.26	—
DeformableGS Yang et al. (2024)	28.82	0.898	0.173	1.898	0.697	—	—	1.299	12.90	—
LiDAR-RT Zhou et al. (2025)	—	—	—	0.003	0.046	0.056	**0.946**	0.176	—	0.93
UniSim Yang et al. (2023b)	24.70	0.799	0.247	0.023	0.055	0.072	0.823	0.671	8.77	1.06
NeuRAD Tonderski et al. (2024)	29.61	0.853	**0.148**	0.005	0.081	0.054	0.875	0.199	9.89	1.19
SplatAD (Hess et al., 2025)	30.60	0.900	0.150	0.008	0.025	0.055	0.866	0.223	52.28	2.94
SimULi	**32.35**	**0.922**	0.150	**0.002**	**0.019**	**0.053**	0.932	**0.148**	**179.45**	**10.56**

4.1 Static Environments

Dataset. We perform experiments on all four scenes of the *Waymo Interp.* benchmark (Huang et al., 2023) and follow the suggested protocol of holding out every 5th frame for validation. We use the front three cameras and render images and LiDAR scans at full resolution.

Baselines. We compare SimULi to Nerfacto (Tancik et al., 2023) as a state-of-the-art NeRF approach and adapt 3DGUT (Wu et al., 2025b) to take LiDAR depth as supervision in the form of sparse depth maps. We also compare to 3DGRT (Moenne-Loccoz et al., 2024), AV-centric methods in `drivestudio` (Chen et al., 2025; Yan et al., 2024; Chen et al., 2023; Yang et al., 2024) and LiDAR-RT (Zhou et al., 2025) as a LiDAR-only particle ray tracing method. We further measure SplatAD (Hess et al., 2025), NeuRAD (Tonderski et al., 2024) and `neurad-studio`'s UniSim (Yang et al., 2023b) implementation as joint camera-LiDAR baselines, along with the official AlignMiF (Tang et al., 2024) implementation as a NeRF-based method that also addresses camera-LiDAR misalignment in static scenes.

Metrics. We evaluate image quality through PSNR, SSIM (Wang et al., 2004), and the AlexNet variant of LPIPS (Zhang et al., 2018). We list the median absolute depth error, mean relative depth accuracy, and chamfer distance of LiDAR predictions in meters, and intensity and ray drop accuracy for methods that support it. As 3DGRT and LiDAR-RT need ray tracing cores, we measure camera and LiDAR rendering speed (denoted in millions of pixels/rays per second) on an NVIDIA A40.

Results. We present results in Table 1, qualitative examples in Fig. 5, and videos in the supplement. Visually, SimULi outperforms all methods by $>$2dB PSNR, and is best or nearly-best across all other metrics. It outperforms LiDAR-RT (Zhou et al., 2025), which solely targets LiDAR reconstruction, on all metrics except ray drop accuracy (for which LiDAR-RT uses a U-Net refinement network) and renders $>10\times$ faster. Although our camera rendering builds upon 3DGUT (Wu et al., 2025b), the improvements in our pipeline (anchoring, appearance variation, environment map) improve rendering quality by 3dB PSNR and produce fewer "floaters", leading to slightly faster render-

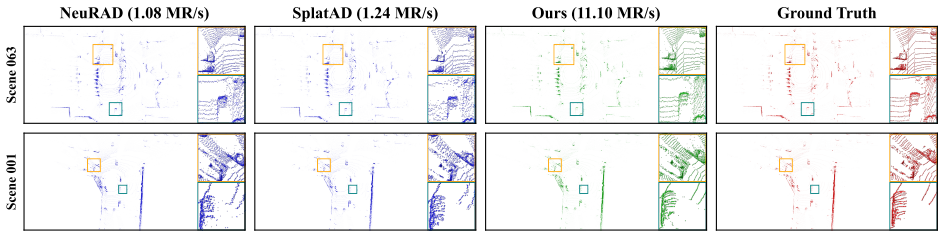

Figure 7: **PandaSet.** SimULi renders the fastest by >10×. Compared to other joint camera-LiDAR methods, ours provides the sharpest LiDAR renderings, especially near vehicles.

Table 3: **PandaSet Reconstruction.** We outperform all prior work by a wide margin, improving upon the second-best method (SplatAD) by >1dB PSNR while rendering camera views 60% faster.

Method	PSNR↑	SSIM↑	LPIPS↓	MedL2. ↓	MeanRelL2↓	Int. RMSE↓	RayDrop↑	CD ↓	MP/s↑	MR/s↑
OmniRe (Chen et al., 2025)	25.82	0.779	0.322	0.131	0.083	—	—	0.970	56.03	—
StreetGS (Yan et al., 2024)	25.82	0.780	0.319	0.162	0.079	—	—	1.012	68.31	—
PVG (Chen et al., 2023)	24.71	0.723	0.464	39.859	0.593	—	—	6.763	24.88	—
DeformableGS (Yang et al., 2024)	25.00	0.770	0.349	0.359	0.159	—	—	0.289	16.52	—
UniSim (Yang et al., 2023b)	23.53	0.693	0.334	0.047	0.079	0.087	0.917	1.326	10.05	1.07
NeuRAD (Tonderski et al., 2024)	26.50	0.767	0.241	0.006	0.054	0.055	0.973	0.321	9.71	1.10
SplatAD (Hess et al., 2025)	28.58	0.878	**0.186**	0.010	0.032	0.054	0.974	0.336	86.74	1.22
SimULi	**29.76**	**0.881**	0.195	**0.002**	**0.006**	**0.034**	**0.997**	**0.206**	**137.74**	**11.10**

ing. Compared to AlignMiF (Tang et al., 2024), which addresses camera-LiDAR misalignment via feature fusion that incurs a large inference-time cost, our factorization instead improves rendering speed (as we only rasterize the subset of Gaussians relevant to the sensor being rendered).

4.2 Dynamic Environments

Datasets and Baselines. We measure reconstruction on the same PandaSet scenes as SplatAD (Hess et al., 2025) and novel view synthesis on both PandaSet and the *Waymo Dynamic* benchmark (Wu et al., 2024). We compare to the methods in Sec. 4.1 that handle dynamics.

Metrics. We evaluate *Waymo Dynamic* with the same metrics used in Sec. 4.1. On PandaSet, we measure timings on 80GB NVIDIA A100 GPUs to ensure that our comparisons are as close as possible to the setting described in SplatAD (Hess et al., 2025), the baseline closest to our work.

Results. We list reconstruction results in Table 3 and novel view synthesis in Tables 2 and 7. We provide camera visuals in Figs. 6 and 14, LiDAR in Figs. 7 and 13, and videos in the supplement. In all cases, SimULi provides the best visual and depth quality. Compared to SplatAD (Hess et al., 2025), the method closest to ours, we improve PSNR by 0.4-1.7 dB without relying on CNNs for view dependence, render cameras 1.5-3× faster, and accelerate LiDAR by 14×.

4.3 Diagnostics

Representation. We compare our factorized model to the alternative of encoding all sensors into a single particle set and vary the strength of LiDAR depth loss λ_d (Fig. 4). We also ablate the bilateral grids and environment map used to improve camera rendering. We summarize results in Table 4. Not only does anchoring improve NVS compared to camera-only reconstruction ($\lambda_d = 0$), but it outperforms the unified strategy across all metrics for all values of λ_d, and renders LiDAR 2× faster. Bilateral grids and environment maps improve camera quality to different degrees.

LiDAR Rendering. We measure rendering speed on a single scene while varying the maximum number of points per tile M and the number of elevation tiles N_ϕ. The choice $M = 32, N_\phi = 16$ gives the best LiDAR rendering speed (note that does not affect quality). This highlights the benefits of our automated strategy - we can easily find optimal settings for any sensor via straightforward grid search, instead of manually specifying tile boundaries as in prior work (Hess et al., 2025).

5 CONCLUSION

We propose SimULi, the first method that renders arbitrary camera models and LiDAR sensors in real-time. Our automated LiDAR tiling and ray-based culling accelerate rendering $>10\times$ relative to prior work. Our factorized representation greatly improves multi-sensor reconstruction quality and is of interest to many downstream applications.

Table 4: **Ablations.** NVS metrics averaged across PandaSet.

Method	Factorized Gaussians	Bilateral Grid	Env. Map	PSNR↑	CD↓	MP/s↑	MR/s↑
Direct $\lambda_d = 0$	✗	✓	✓	26.61	6.248	134.75	5.55
Direct $\lambda_d = 0.001$	✗	✓	✓	<u>26.70</u>	0.718	128.22	5.01
Direct $\lambda_d = 0.01$	✗	✓	✓	26.39	0.475	132.45	4.97
Direct $\lambda_d = 0.1$	✗	✓	✓	25.78	0.393	131.04	4.77
w/o Bilateral Grid	✓	✗	✓	25.99	0.337	<u>130.63</u>	**12.07**
w/o Env. Map	✓	✓	✗	<u>26.81</u>	<u>0.336</u>	125.30	<u>11.83</u>
Full Method	✓	✓	✓	**27.12**	**0.331**	**136.33**	11.02

Table 5: **LiDAR Tiling (MR/s).**

$N_\phi \setminus M$	256	128	64	32
64	6.96	7.22	12.29	14.24
32	5.48	7.89	13.87	13.51
16	6.49	12.02	13.64	**15.75**
8	9.24	9.24	10.05	15.12

6 ETHICS STATEMENT

Our approach facilitates the creation and rendering of high-fidelity neural representations. Consequently, the inherent risks mirror those found in other neural rendering research, mainly concerning privacy and security due to the potential capture of sensitive information, whether intentional or not. These concerns are particularly relevant in autonomous vehicle settings, which our method targets, as training data may contain private details like human faces and vehicle license numbers. A potential solution would be to incorporate semantic distillation into the model's representation, as seen in prior work (Kobayashi et al., 2022; Tschernezki et al., 2022; Turki et al., 2023; Kerr et al., 2023), to filter out sensitive data during rendering. However, this information would still persist within the model itself. A more effective mitigation strategy would be to preprocess the input data used to train the model before it is ever ingested (Wang et al., 2017).

7 REPRODUCIBILITY STATEMENT

We describe how to build our pipeline in the paper and appendix, provide pseudo-code for our LiDAR tiling and culling strategies, list our training hyperparameters, and detail our experimental protocol. All data used for evaluation is publicly available.

REFERENCES

Sai Praveen Bangaru, Lifan Wu, Tzu-Mao Li, Jacob Munkberg, Gilbert Bernstein, Jonathan Ragan-Kelley, Frédo Durand, Aaron Lefohn, and Yong He. Slang.d: Fast, modular and differentiable shader programming. *ACM Trans. Graph.*, 42(6), December 2023. ISSN 0730-0301. doi: 10.1145/3618353. URL https://doi.org/10.1145/3618353.

Holger Caesar, Varun Bankiti, Alex H. Lang, Sourabh Vora, Venice Erin Liong, Qiang Xu, Anush Krishnan, Yu Pan, Giancarlo Baldan, and Oscar Beijbom. nuscenes: A multimodal dataset for autonomous driving. In *CVPR*, 2020.

Yurui Chen, Chun Gu, Junzhe Jiang, Xiatian Zhu, and Li Zhang. Periodic vibration gaussian: Dynamic urban scene reconstruction and real-time rendering. *arXiv preprint arXiv:2311.18561*, 2023.

Ziyu Chen, Jiawei Yang, Jiahui Huang, Riccardo de Lutio, Janick Martinez Esturo, Boris Ivanovic, Or Litany, Zan Gojcic, Sanja Fidler, Marco Pavone, Li Song, and Yue Wang. Omnire: Omni urban scene reconstruction. In *ICLR*, 2025.

Tobias Fischer, Samuel Rota Bulò, Yung-Hsu Yang, Nikhil Varma Keetha, Lorenzo Porzi, Norman Müller, Katja Schwarz, Jonathon Luiten, Marc Pollefeys, and Peter Kontschieder. FlowR: Flowing from sparse to dense 3d reconstructions. *arXiv preprint arXiv:2504.01647*, 2025.

Jianfei Guo, Nianchen Deng, Xinyang Li, Yeqi Bai, Botian Shi, Chiyu Wang, Chenjing Ding, Dongliang Wang, and Yikang Li. Streetsurf: Extending multi-view implicit surface reconstruction to street views. *arXiv preprint arXiv:2306.04988*, 2023.

Georg Hess, Carl Lindström, Maryam Fatemi, Christoffer Petersson, and Lennart Svensson. Splatad: Real-time lidar and camera rendering with 3d gaussian splatting for autonomous driving. In *CVPR*, 2025.

Shengyu Huang, Zan Gojcic, Zian Wang, Francis Williams, Yoni Kasten, Sanja Fidler, Konrad Schindler, and Or Litany. Neural lidar fields for novel view synthesis. In *ICCV*, 2023.

Junzhe Jiang, Chun Gu, Yurui Chen, and Li Zhang. Gs-lidar: Generating realistic lidar point clouds with panoramic gaussian splatting. In *ICLR*, 2025.

Bernhard Kerbl, Georgios Kopanas, Thomas Leimkühler, and George Drettakis. 3d gaussian splatting for real-time radiance field rendering. *ACM Transactions on Graphics*, 42(4), July 2023. URL https://repo-sam.inria.fr/fungraph/3d-gaussian-splatting/.

Justin* Kerr, Chung Min* Kim, Ken Goldberg, Angjoo Kanazawa, and Matthew Tancik. Lerf: Language embedded radiance fields. In *ICCV*, 2023.

Shakiba Kheradmand, Daniel Rebain, Gopal Sharma, Weiwei Sun, Yang-Che Tseng, Hossam Isack, Abhishek Kar, Andrea Tagliasacchi, and Kwang Moo Yi. 3d gaussian splatting as markov chain monte carlo. *Advances in Neural Information Processing Systems*, 37:80965–80986, 2024.

Sosuke Kobayashi, Eiichi Matsumoto, and Vincent Sitzmann. Decomposing nerf for editing via feature field distillation. In *Advances in Neural Information Processing Systems*, volume 35, 2022.

Yiyi Liao, Jun Xie, and Andreas Geiger. KITTI-360: A novel dataset and benchmarks for urban scene understanding in 2d and 3d. *arXiv preprint arXiv:2109.13410*, 2021.

Ben Mildenhall, Pratul P. Srinivasan, Matthew Tancik, Jonathan T. Barron, Ravi Ramamoorthi, and Ren Ng. NeRF: Representing scenes as neural radiance fields for view synthesis. In *ECCV*, 2020.

Nicolas Moenne-Loccoz, Ashkan Mirzaei, Or Perel, Riccardo de Lutio, Janick Martinez Esturo, Gavriel State, Sanja Fidler, Nicholas Sharp, and Zan Gojcic. 3d gaussian ray tracing: Fast tracing of particle scenes. *ACM Transactions on Graphics and SIGGRAPH Asia*, 2024.

Thomas Müller, Alex Evans, Christoph Schied, and Alexander Keller. Instant neural graphics primitives with a multiresolution hash encoding. *ACM Trans. Graph.*, 41(4):102:1–102:15, July 2022. doi: 10.1145/3528223.3530127. URL https://doi.org/10.1145/3528223.3530127.

Julian Ost, Fahim Mannan, Nils Thuerey, Julian Knodt, and Felix Heide. Neural scene graphs for dynamic scenes. In *Proceedings of the IEEE/CVF Conference on Computer Vision and Pattern Recognition (CVPR)*, pp. 2856–2865, June 2021.

A Paszke. Pytorch: An imperative style, high-performance deep learning library. *arXiv preprint arXiv:1912.01703*, 2019.

Konstantinos Rematas, Andrew Liu, Pratul P. Srinivasan, Jonathan T. Barron, Andrea Tagliasacchi, Tom Funkhouser, and Vittorio Ferrari. Urban radiance fields. 2022.

Michael Steiner, Thomas Köhler, Lukas Radl, Felix Windisch, Dieter Schmalstieg, and Markus Steinberger. Aaa-gaussians: Anti-aliased and artifact-free 3d gaussian rendering, 2025. URL https://arxiv.org/abs/2504.12811.

Pei Sun, Henrik Kretzschmar, Xerxes Dotiwalla, Aurelien Chouard, Vijaysai Patnaik, Paul Tsui, James Guo, Yin Zhou, Yuning Chai, Benjamin Caine, Vijay Vasudevan, Wei Han, Jiquan Ngiam, Hang Zhao, Aleksei Timofeev, Scott Ettinger, Maxim Krivokon, Amy Gao, Aditya Joshi, Yu Zhang, Jonathon Shlens, Zhifeng Chen, and Dragomir Anguelov. Scalability in perception for autonomous driving: Waymo open dataset. In *CVPR*, June 2020.

Matthew Tancik, Ethan Weber, Evonne Ng, Ruilong Li, Brent Yi, Justin Kerr, Terrance Wang, Alexander Kristoffersen, Jake Austin, Kamyar Salahi, Abhik Ahuja, David McAllister, and Angjoo Kanazawa. Nerfstudio: A modular framework for neural radiance field development. In *ACM SIGGRAPH 2023 Conference Proceedings*, SIGGRAPH '23, 2023.

Tao Tang, Guangrun Wang, Yixing Lao, Peng Chen, Jie Liu, Liang Lin, Kaicheng Yu, and Xiaodan Liang. Alignmif: Geometry-aligned multimodal implicit field for lidar-camera joint synthesis. 2024.

Tang Tao, Longfei Gao, Guangrun Wang, Yixing Lao, Peng Chen, Zhao hengshuang, Dayang Hao, Xiaodan Liang, Mathieu Salzmann, and Kaicheng Yu. Lidar-nerf: Novel lidar view synthesis via neural radiance fields. *arXiv preprint arXiv:2304.10406*, 2023.

Adam Tonderski, Carl Lindström, Georg Hess, William Ljungbergh, Lennart Svensson, and Christoffer Petersson. Neurad: Neural rendering for autonomous driving. In *CVPR*, pp. 14895–14904, 2024.

Vadim Tschernezki, Iro Laina, Diane Larlus, and Andrea Vedaldi. Neural Feature Fusion Fields: 3D distillation of self-supervised 2D image representation. In *Proceedings of the International Conference on 3D Vision (3DV)*, 2022.

Haithem Turki, Jason Y Zhang, Francesco Ferroni, and Deva Ramanan. Suds: Scalable urban dynamic scenes. In *Computer Vision and Pattern Recognition (CVPR)*, 2023.

Haithem Turki, Vasu Agrawal, Samuel Rota Bulò, Lorenzo Porzi, Peter Kontschieder, Deva Ramanan, Michael Zollhöfer, and Christian Richardt. Hybridnerf: Efficient neural rendering via adaptive volumetric surfaces. In *Computer Vision and Pattern Recognition (CVPR)*, 2024.

Junjue Wang, Brandon Amos, Anupam Das, Padmanabhan Pillai, Norman Sadeh, and Mahadev Satyanarayanan. A scalable and privacy-aware IoT service for live video analytics. In *Multimedia Systems Conference*, pp. 38–49, 2017.

Yuehao Wang, Chaoyi Wang, Bingchen Gong, and Tianfan Xue. Bilateral guided radiance field processing. *ACM Transactions on Graphics (TOG)*, 43(4):1–13, 2024.

Zhou Wang, A.C. Bovik, H.R. Sheikh, and E.P. Simoncelli. Image quality assessment: from error visibility to structural similarity. *IEEE Transactions on Image Processing*, 13(4):600–612, 2004. doi: 10.1109/TIP.2003.819861.

Zian Wang, Tianchang Shen, Merlin Nimier-David, Nicholas Sharp, Jun Gao, Alexander Keller, Sanja Fidler, Thomas Müller, and Zan Gojcic. Adaptive shells for efficient neural radiance field rendering. *ACM Trans. Graph.*, 42(6), 2023. doi: 10.1145/3618390. URL https://doi.org/10.1145/3618390.

Benjamin Wilson, William Qi, Tanmay Agarwal, John Lambert, Jagjeet Singh, Siddhesh Khandelwal, Bowen Pan, Ratnesh Kumar, Andrew Hartnett, Jhony Kaesemodel Pontes, Deva Ramanan, Peter Carr, and James Hays. Argoverse 2: Next generation datasets for self-driving perception and forecasting. In *Proceedings of the Neural Information Processing Systems Track on Datasets and Benchmarks (NeurIPS Datasets and Benchmarks 2021)*, 2021.

Hanfeng Wu, Xingxing Zuo, Stefan Leutenegger, Or Litany, Konrad Schindler, and Shengyu Huang. Dynamic lidar re-simulation using compositional neural fields. In *CVPR*, 2024.

Jay Zhangjie Wu, Yuxuan Zhang, Haithem Turki, Xuanchi Ren, Jun Gao, Mike Zheng Shou, Sanja Fidler, Zan Gojcic, and Huan Ling. Difix3d+: Improving 3d reconstructions with single-step diffusion models. 2025a.

Qi Wu, Janick Martinez Esturo, Ashkan Mirzaei, Nicolas Moenne-Loccoz, and Zan Gojcic. 3dgut: Enabling distorted cameras and secondary rays in gaussian splatting. In *CVPR*, 2025b.

Pengchuan Xiao, Zhenlei Shao, Steven Hao, Zishuo Zhang, Xiaolin Chai, Judy Jiao, Zesong Li, Jian Wu, Kai Sun, Kun Jiang, Yunlong Wang, and Diange Yang. Pandaset: Advanced sensor suite dataset for autonomous driving. In *2021 IEEE International Intelligent Transportation Systems Conference (ITSC)*, pp. 3095–3101. IEEE Press, 2021. doi: 10.1109/ITSC48978.2021.9565009. URL https://doi.org/10.1109/ITSC48978.2021.9565009.

Ziyang Xie, Junge Zhang, Wenye Li, Feihu Zhang, and Li Zhang. S-nerf: Neural radiance fields for street views. In *International Conference on Learning Representations (ICLR)*, 2023.

Yunzhi Yan, Haotong Lin, Chenxu Zhou, Weijie Wang, Haiyang Sun, Kun Zhan, Xianpeng Lang, Xiaowei Zhou, and Sida Peng. Street gaussians: Modeling dynamic urban scenes with gaussian splatting. In *ECCV*, 2024.

Jiawei Yang, Boris Ivanovic, Or Litany, Xinshuo Weng, Seung Wook Kim, Boyi Li, Tong Che, Danfei Xu, Sanja Fidler, Marco Pavone, and Yue Wang. Emernerf: Emergent spatial-temporal scene decomposition via self-supervision. *arXiv preprint arXiv:2311.02077*, 2023a.

Ze Yang, Yun Chen, Jingkang Wang, Sivabalan Manivasagam, Wei-Chiu Ma, Anqi Joyce Yang, and Raquel Urtasun. Unisim: A neural closed-loop sensor simulator. In *CVPR*, 2023b.

Ziyi Yang, Xinyu Gao, Wen Zhou, Shaohui Jiao, Yuqing Zhang, and Xiaogang Jin. Deformable 3d gaussians for high-fidelity monocular dynamic scene reconstruction. In *CVPR*, 2024.

Zehao Yu, Anpei Chen, Binbin Huang, Torsten Sattler, and Andreas Geiger. Mip-splatting: Alias-free 3d gaussian splatting. In *Proceedings of the IEEE/CVF Conference on Computer Vision and Pattern Recognition (CVPR)*, pp. 19447–19456, June 2024.

Junge Zhang, Feihu Zhang, Shaochen Kuang, and Li Zhang. Nerf-lidar: Generating realistic lidar point clouds with neural radiance fields. In *AAAI*, 2024.

Richard Zhang, Phillip Isola, Alexei A Efros, Eli Shechtman, and Oliver Wang. The unreasonable effectiveness of deep features as a perceptual metric. In *CVPR*, 2018.

Zehan Zheng, Fan Lu, Weiyi Xue, Guang Chen, and Changjun Jiang. Lidar4d: Dynamic neural fields for novel space-time view lidar synthesis. In *CVPR*, 2024.

Chenxu Zhou, Lvchang Fu, Sida Peng, Yunzhi Yan, Zhanhua Zhang, Yong Chen, Jiazhi Xia, and Xiaowei Zhou. LiDAR-RT: Gaussian-based ray tracing for dynamic lidar re-simulation. In *CVPR*, 2025.

Xiaoyu Zhou, Zhiwei Lin, Xiaojun Shan, Yongtao Wang, Deqing Sun, and Ming-Hsuan Yang. Drivinggaussian: Composite gaussian splatting for surrounding dynamic autonomous driving scenes. In *Proceedings of the IEEE/CVF Conference on Computer Vision and Pattern Recognition*, pp. 21634–21643, 2024.

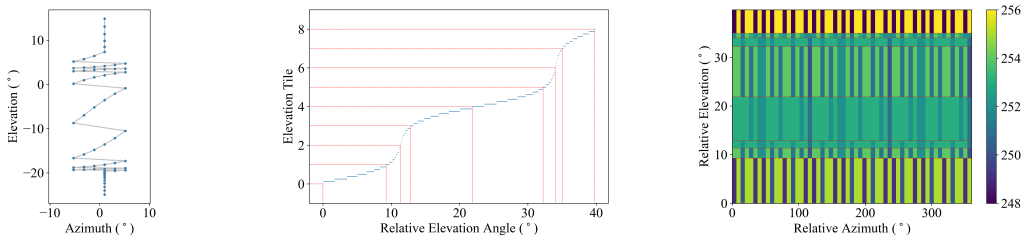

(a) Beam pattern (b) Elevation angle to tile map (c) Beam count per tile

Figure 8: **Customized LiDAR Model.** We can readily apply our automated tiling strategy to arbitrary spinning LiDAR models.

A VIDEOS

We include several videos as supplementary materials under the '**vids**' folder. We recommend watching these videos via '**index.html**', which also includes descriptions and further details on the results and comparisons.

B LIDAR TILING

We describe our LiDAR tiling strategy in Procedure 1. As discussed in Sec. 4.3, a significant advantage of this approach is that it readily be applied to any spinning LiDAR model to find optimal tiling parameters, including the customized model shown in Fig. 8, instead of manual exploration as in prior methods (Hess et al., 2025).

Algorithm 1 ELEVATIONTILING

Input: elevation angles: $\boldsymbol{\Phi}$, elevation tile count N_ϕ, maximum point count per tile M
Output: numbers of azimuth tiles: N_θ, elevation tiling: $\boldsymbol{T}$

$r = 400$ ▷ *pre-defined elevation resolution*
$\boldsymbol{H} = \text{Histogram}(\boldsymbol{\Phi}, \text{nbins} = r)$ ▷ *compute histogram of elevations*
$\boldsymbol{C} = \text{CumulativeSum}(\boldsymbol{H})$ ▷ *compute cumulative sum of histogram*
$\boldsymbol{C} = \boldsymbol{C} / \boldsymbol{C}_{\max} \cdot N_\phi$
$\boldsymbol{T} = \{0\}$ ▷ *compute elevation tiling iteratively based on $\boldsymbol{C}$*
$b = 1$
for $i = 0$ to $N_\phi - 1$ **do**
  if $\boldsymbol{C}(i) \geq b$ **then**
    $\boldsymbol{T}$.append(i)
    b += 1
$\boldsymbol{T} = \boldsymbol{T} / r \cdot (\Phi_{\max} - \Phi_{\min})$ ▷ *normalize tiling $\boldsymbol{T}$*
$\boldsymbol{H} = \text{Histogram}(\boldsymbol{\Phi}, \text{bins} = \boldsymbol{T})$ ▷ *re-compute histogram based on newly computed tiling $\boldsymbol{T}$*
$N_\theta = \boldsymbol{H}_{\max} \,/\, M$ ▷ *compute the number of azimuth tiles based on constraint M*
return $N_\theta, \boldsymbol{T}$

C RAY-BASED CULLING

We profile our ray-based culling in Table 6. The constant-time filtering adds a small overhead (about 2%) that is offset by subsequent speedups to sorting and rendering (8-9%). We compute the number of ray occupancies for each particle as described in Procedure 2 and subsequently use it to filter projections as described in Procedure 3.

Algorithm 2 RAYOCCUPANCYCOUNT

Input: rectangular extents $\boldsymbol{E}_t$, particle center $\boldsymbol{p}$,
summed-area table of ray mask $\boldsymbol{S}_{\text{ray}}$
Output: number of ray occupancies inside the extents n

$\boldsymbol{I}_{ll} = \boldsymbol{p} - \boldsymbol{E}_t$ ▷*lower left dense tile indices*
$\boldsymbol{I}_{ur} = \boldsymbol{p} + \boldsymbol{E}_t$ ▷*upper right dense tile indices*
▷*Compute ray occupancy counts using the summed-area table*
$A = \boldsymbol{S}_{\text{ray}}[\boldsymbol{I}_{ur}.x + 1, \boldsymbol{I}_{ur}.y + 1]$
$B = \boldsymbol{S}_{\text{ray}}[\boldsymbol{I}_{ll}.x, \boldsymbol{I}_{ur}.y + 1]$
$C = \boldsymbol{S}_{\text{ray}}[\boldsymbol{I}_{ur}.x + 1, \boldsymbol{I}_{ll}.y]$
$D = \boldsymbol{S}_{\text{ray}}[\boldsymbol{I}_{ll}.x, \boldsymbol{I}_{ll}.y]$
$n = A - B - C + D$
return n

Algorithm 3 PROJECTPARTICLES

Input: culling tile extents $\boldsymbol{E}_t$, rendering tile extents $\boldsymbol{E}_r$, particle center $\boldsymbol{p}$,
summed-area table of ray mask $\boldsymbol{S}_{\text{ray}}$
Output: coarse tile count n

$n = 0$
if RayOccupancyCount($\boldsymbol{E}_t$, $\boldsymbol{p}$, $\boldsymbol{S}_{\text{ray}}$) > 0 **then**
  for $x = 1$ to $\boldsymbol{E}_r.x$ **do**
    for $y = 1$ to $\boldsymbol{E}_r.y$ **do**
      $n = n + 1$
return n

D ANTI-ALIASING FOR BEAM DIVERGENCE

As mentioned in Sec. 3.2, we apply a 3D smoothing filter to LiDAR Gaussians in G_l similar to that used for camera anti-aliasing in AAA-Gaussians (Steiner et al., 2025) that scales its covariance:

$$\hat{\rho}_{\perp}(\mathbf{x}) = \sqrt{\frac{|\Sigma_{\perp}|}{|\hat{\Sigma}_{\perp}|}} \exp(-\frac{1}{2}(\mathbf{x}-\mu)^{\top}\hat{\Sigma}^{-1}(\mathbf{x}-\mu)) \,, \tag{6}$$

where $\mathbf{d}$ is the normalized vector between μ and the camera origin $\mathbf{o}$, and $\Sigma_{\perp}$ denotes the 2×2 projected onto the subspace orthogonal to $\mathbf{d}$. However, unlike AAA-Gaussians and prior work (Yu et al., 2024), we do not scale the opacity factor $\sqrt{\frac{|\Sigma_{\perp}|}{|\hat{\Sigma}_{\perp}|}}$. Although this change can be seen as straightforward, we found it to have a significant impact on LiDAR reconstruction (and depth data more broadly) as the filter otherwise degrades scene geometry by encouraging blending foreground and background objects. Fig. 9 illustrates the differences in approaches.

E IMPLEMENTATION DETAILS

We train our model in the Pytorch framework (Paszke, 2019) and use custom CUDA and Slang (Bangaru et al., 2023) kernels for rendering. We initialize each scene by voxelizing the LiDAR point cloud with a resolution of 0.1 meters. We project the point cloud onto the camera images and initialize the color and scale of each Gaussian with the color and pixel footprint of the closest image. We train on each scene for 30,000 iterations and use a variant of MCMC's densification strategy (Kheradmand et al., 2024) that relocates Gaussians based on reconstruction error instead of opacity. This slightly improves reconstruction quality and combines better with the entropy loss that we apply to Gaussians in G_l (as relocation would otherwise skew towards the binarized high-opacity Gaussians the loss encourages).

To generate plausible renderings at novel timestamps, we encourage smoothness across our affine color transformations $\mathcal{A}$ and environment map via a total variation loss (Wang et al., 2024) $\mathcal{L}_{\text{TV}}$ and identity drift loss $\mathcal{L}_{\text{drift}}$. We also regularize the scale and opacity of our Gaussians as in

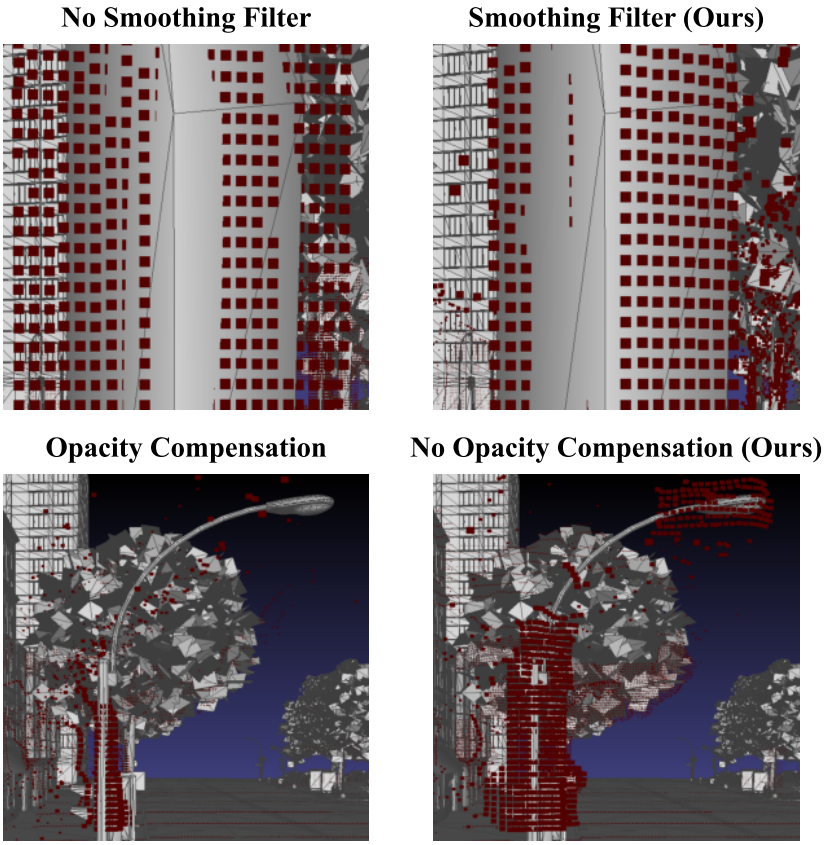

Figure 9: **Beam Divergence.** We show a representative example where LiDAR divergence causes "bloating" (**top-left**) that our filter removes (**top-right**). We crucially omit the opacity compensation used in prior work (Steiner et al., 2025; Yu et al., 2024) as it blends foreground and background objects, adversely affecting the recovered street lamp geometry (**bottom**).

Table 6: **Ray-based Culling.** We measure kernel run times in milliseconds. Our filtering incurs a small constant time cost offset by improvements to the subsequent sort and render operations.

Kernels	w/ Ray Culling	w/o Ray Culling	Speedup (%)
Project	2.43	2.39	-1.71
Sort	0.48	0.52	7.67
Render	4.71	5.17	9.02

Table 7: **PandaSet NVS.** Similar to Table 3, SimULi renders the fastest, provides the best PSNR, and outperforms next-best method SplatAD across every LiDAR metric.

Method	PSNR↑	SSIM↑	LPIPS↓	MedL2. ↓	MeanRelL2↓	Int. RMSE↓	RayDrop↑	CD ↓	MP/s↑	MR/s↑
OmniRe (Chen et al., 2025)	25.13	0.757	0.351	0.425	0.113	—	—	1.126	53.19	—
StreetGS (Yan et al., 2024)	25.09	0.756	0.352	0.378	0.102	—	—	1.218	64.67	—
PVG (Chen et al., 2023)	24.00	0.709	0.462	30.686	0.563	—	—	5.793	23.68	—
DeformableGS (Yang et al., 2024)	23.68	0.720	0.346	0.190	0.182	—	—	1.057	15.81	—
UniSim (Yang et al., 2023b)	23.50	0.693	0.328	0.065	0.120	0.087	0.919	1.438	11.25	0.87
NeuRAD (Tonderski et al., 2024)	25.97	0.759	0.243	0.009	0.075	0.062	0.963	0.360	11.37	1.08
SplatAD (Hess et al., 2025)	26.73	0.815	**0.193**	0.011	0.035	**0.059**	0.966	0.346	88.79	1.24
SimULi	**27.12**	**0.830**	0.220	**0.006**	**0.018**	**0.059**	**0.970**	**0.331**	**136.33**	**11.02**

MCMC (Kheradmand et al., 2024), which we found to improve rendering quality. Our overall regularization is thus:

$$\mathcal{L}_{\text{reg}} \coloneqq \mathcal{L}_{\text{entropy}} + \mathcal{L}_{\text{TV}} + \lambda_{\text{drift}}\mathcal{L}_{\text{drift}} + \lambda_{\mathbf{\Sigma}} \sum_{ij} \sqrt{\text{eig}_j(\mathbf{\Sigma}_i)} + \lambda_\sigma \sum_i \sigma_i, \tag{7}$$

with $\lambda_{\text{drift}} = 0.001$, $\lambda_{\mathbf{\Sigma}} = 0.001$, and $\lambda_\sigma = 0.005$ in our experiments.

F Limitations

SimULi does not currently model non-rigid objects, although solutions such as Chen et al. (2025) are directly applicable to our method. As with other scene optimization methods, novel view synthesis suffers when rendering viewpoints that greatly deviate from the training poses, which could be mitigated via generative priors as proposed in Wu et al. (2025a); Fischer et al. (2025). Finally, the K nearest neighbors calculations used in the anchoring loss adds a modest training time overhead (around 14 minutes with our default settings). This could be further reduced by adjusting K (setting it to 20 decreases the overhead to 6 minutes with little change in quality) or via fused custom CUDA kernels.

G Additional Results and Visualizations

Time-dependent Effects. As discussed in Sec. 3.2, we approximate each Gaussian by projecting 7 sigma points to estimate its 2D conic. As these points are independently projected, we handle time-dependent effects such as rolling shutter and its LiDAR equivalent at high granularity by incorporating sensor movement into the projection function. We illustrate its impact in Fig. 10.

LiDAR Noise. LiDAR sensors tend to exhibit "bloating" artifacts near thin and reflective surfaces. In prior, non-factorized methods, this noisy "ground-truth" supervision degrades either camera quality (due to learning incorrect LiDAR-supervised geometry) or LiDAR fidelity (since LiDAR loss must be down-weighed and is typically applied uniformly across all points). As illustrated in Fig. 11, factorization provides the flexibility needed to capture these effects without impacting camera quality.

LiDAR Projection. We illustrate the validity of our LiDAR projection strategy by comparing it to Monte Carlo sampling, which is more accurate but expensive to compute, in Fig. 12 and measure its

Figure 10: **Rolling Shutter.** Images captured from fast-moving vehicles such as those in the Waymo Open Dataset (Sun et al., 2020) exhibit rolling shutter effects that, when unaccounted for, degrade reconstruction quality (**left**). Our rendering formulation incorporates sensor movement into the projection function and evaluates the particle response function in 3D using the exact timestamp of each ray, allowing us to model time-dependent effects at high granularity (**right**).

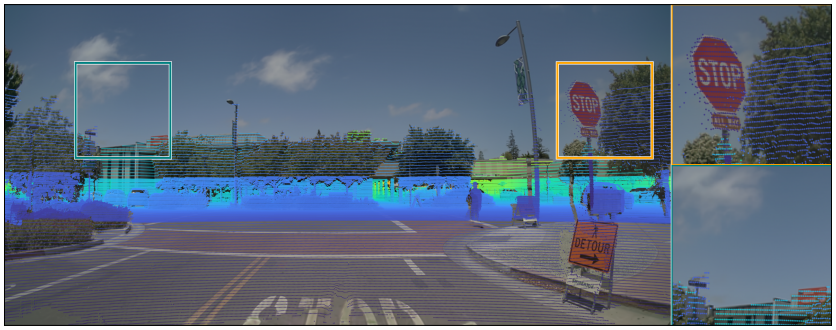

Figure 11: **LiDAR Noise.** LiDAR tends to exhibit "bloating" artifacts near reflective surfaces such as the stop sign (**top inset**) and thin structures (**bottom inset**). Our factorized representation and anchoring loss accurately capture these effects without compromising camera quality.

Table 8: **LiDAR Projection.** We compare our LiDAR projection strategy to linearization and Monte Carlo sampling alternatives. Our results are near-identical to Monte Carlo sampling despite projecting far fewer points per Gaussian.

Method	MedL2. ↓	MeanRelL2↓	Int. RMSE↓	RayDrop↑	CD ↓
Linearization	0.013	0.022	0.053	0.981	0.356
Monte Carlo Sampling	**0.003**	**0.011**	**0.037**	**0.991**	0.252
SimULi	**0.003**	**0.011**	**0.037**	**0.991**	**0.250**

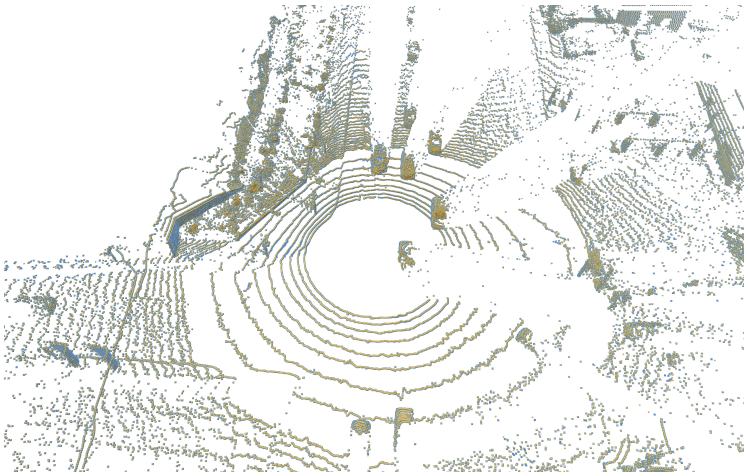

Figure 12: **LiDAR Projection.** We overlay the results of our LiDAR projection function (**orange**) with those generated with Monte Carlo sampling (which is more accurate but expensive to compute) (**blue**). Although our strategy projects far fewer points per Gaussian (7 instead of 200), our results are closely aligned.

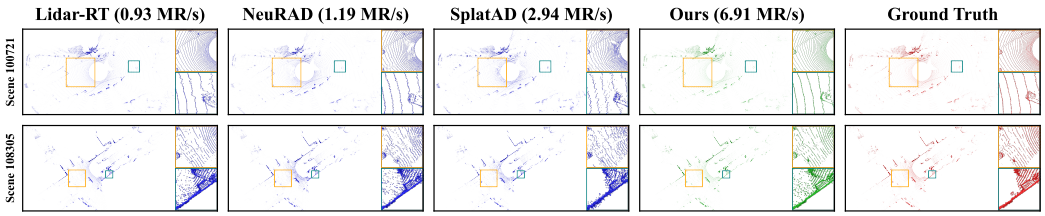

Figure 13: **Waymo Dynamic.** As in Fig. 7, SimULi renders the fastest (as measured on an A40 GPU) and compares favorably to camera-LiDAR and LiDAR-only (Zhou et al., 2025) baselines.

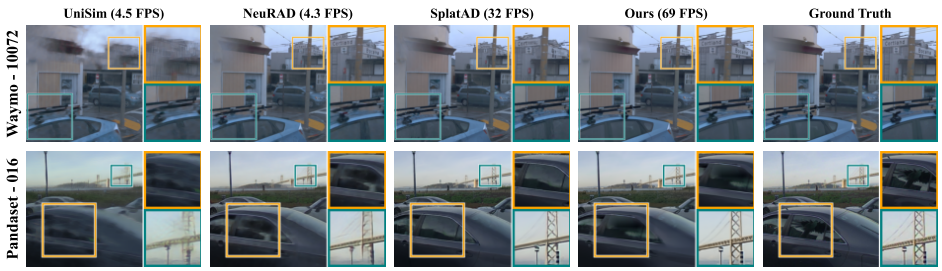

Figure 14: **Additional Scenes.** FPS numbers are averaged across *Waymo Dynamic* and PandaSet. As in Fig. 6, SplatAD's view dependence CNN struggles to reconstruct the sign lettering (**above**). We capture background details and reflections (**below**) better than other methods.

accuracy in Table 8. Our results are near-identical despite projecting far fewer samples per point (7 vs 200).

Baseline Comparisons. We provide results for PandaSet novel view synthesis in Table 7 (which are similar to the findings for reconstruction in Table 3), additional LiDAR renderings on *Waymo Dynamic* in Fig. 13, and camera renderings of dynamic scenes in Fig. 14.